Combustion and Flame 252 (2023) 112429

Contents lists available at ScienceDirect

Combustion and Flame

journal homepage: www.elsevier.com/locate/combustflame

An experimental study of the sooting behavior of a partially premixed flame under moderately rich conditions

Kevin Gleason, Alessandro Gomez*

Yale Center for Combustion Studies, Department of Mechanical Engineering and Materials Science, Yale University, 9 Hillhouse Avenue, 8286, New Haven, CT 06520, USA

ARTICLE INFO

Article history:
Received 29 June 2022
Revised 4 October 2022
Accepted 5 October 2022
Available online 27 March 2023

Keywords:
Soot
Counterflow
Partially premixed flames

ABSTRACT

Soot and its gaseous precursors are quantified in detail (precursors up to 166 amu, volume fraction, particle size, number concentration, and light emissivity dispersion exponent) in a laminar partially premixed counterflow flame of ethylene. The investigated flame has an equivalence ratio $\Phi = 2.43$ and a mixture fraction $Z_{st} = 0.4$, resulting in a distinct double-flame structure consisting of a rich premixed flame component and a diffusion flame component, both stabilized on the fuel side of the stagnation plane. The value of the equivalence ratio makes the premixed flame the dominant contributor to soot production, with soot being oxidized completely by OH from the diffusion flame component. Particle size is measured to increase quasi-monotonically, but remains within a few nanometers throughout the soot forming region. Aromatic species are primarily formed in the post flame region of the premixed flame. Their mole fractions peak close to the premixed flame and decrease as the diffusion flame is approached. The experimentally measured gaseous species are captured well by kinetic models, with the exception of two critical species in soot chemistry: benzene and naphthalene.

1. Introduction

Combustion systems are typically categorized as either premixed or non-premixed (i.e., diffusion controlled), with soot formation being studied separately in either environment in most cases, as reviewed in [1,2]. In practical systems, however, situations arise in which these two regimes coexist in so-called Partially Premixed Flames (PPFs). For example, in compression ignition (CI) engines, fuel and air mix near the injector and form a fuel rich Premixed Flame (PF) with equivalence ratios, Φ, in the range 2–4 and a (non-premixed) Diffusion Flame (DF) structure formed between the premixed flame products and air [3,4]. More generally, PPFs are of relevance under turbulent conditions as a result of turbulent mixing in the partial premixing and stratification of turbulent flames [5,6].

Efforts to quantify the effect of equivalence ratio [7–9], pressure [10], and fuel type [9] on PAH, soot, and NOx emissions were the object of several studies in counterflow PPFs. However, some studies focused on very rich conditions [9,11,12] in which these partially premixed flames can be regarded as perturbations to a diffusion flame and rarely considered the equivalence ratios observed in engines [3,4]. Mungekar and Atreya [11,12] investigated methane partially premixed flames over a range of stoichiometric mixture factions (Z_{st}) under conditions in which the diffusion flame component was positioned either on the oxidizer side or on the fuel side of the stagnation plane. In the former case, soot is formed primarily near the flame front and grows until it is convected away radially at the stagnation plane; in the latter case soot is formed, convected toward the DF component and eventually oxidized [1,13]. Berta et al. [8] investigated a n-heptane flame at an equivalence ratio of $\Phi = 2.5$, quantifying some critical soot precursors, but did not perform soot measurements. Experimentally, studies rarely examine the double flame structure under moderately rich conditions. Yet, under these conditions the hybrid nature of a partially premixed flame arises.

Figure 1 shows a comparison of computed heat release rate profiles, using OPPDIFF in Chemkin Pro (Reaction Design) [14], in a laminar PPFs of ethylene in the counterflow configuration at various equivalence ratios, Φs, in the rich range of the stoichiometry, including a diffusion flame ($\Phi = \infty$). The axial coordinate has the origin chosen at the Gas Stagnation Plane (GSP). Detailed chemistry is modeled with USC-MechII that is known to be optimized for lighter (C1-C4) hydrocarbons: [15]. We held the global strain rate, $(V_{avg,f} + V_{avg,ox})/L$, constant at a value of 45/s, based on mass averaged velocity at the boundaries and burner separation. The stoichiometric mixture fraction, Z_{st} of the DF component was also kept constant. It is based on the mass fraction of oxygen in the oxidizer

* Corresponding author.
E-mail address: alessandro.gomez@yale.edu (A. Gomez).

https://doi.org/10.1016/j.combustflame.2022.112429
0010-2180/

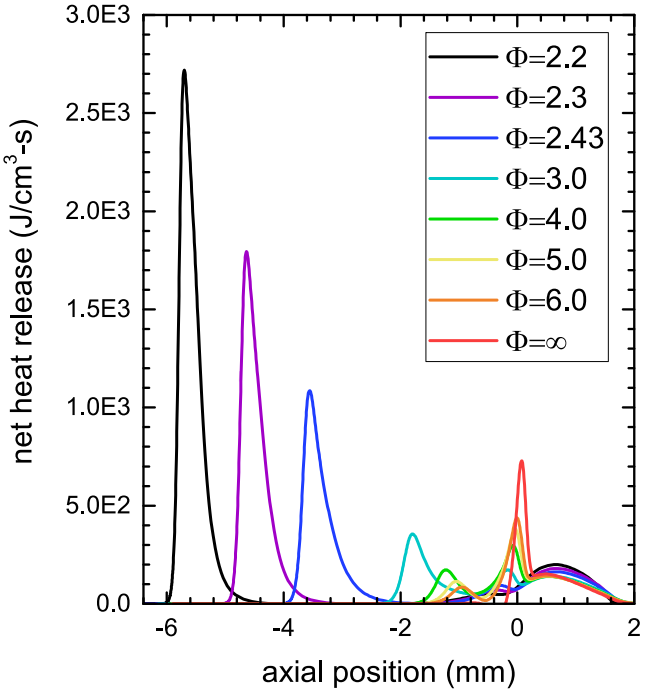

Fig. 1. Computed heat release profiles of partially premixed flames for ethylene mole fraction, mixture fraction and global strain rate constant at 0.17, 0.40 and 45 s^{-1}, respectively.

stream (Y_{OO}) and of the *residual* fuel, Y_{rf}, that is, unburnt C_2H_4, after complete conversion to CO_2 and H_2O from the PF component, resulting in $Z_{st} = (1 + s\ Y_{rf}/Y_{OO})^{-1} = 0.40$. The gas stagnation plane (GSP) and particle stagnation plane (PSP) virtually coincide, and are positioned at z = 0 mm in Fig. 1. The DF is positioned near the GSP and slightly on the fuel side.

We notice the sharp peak of heat release on the left of the origin, for the case of a robust premixed flame that stabilizes upstream of the GSP on the fuel side of the feed stream. The modest secondary peak at the right of the GSP is associated with $CO \rightarrow CO_2$ and $H_2 \rightarrow H_2O$ conversion. As the equivalence ratio increases, the primary peak becomes less pronounced, moves to the right, approaching the GSP, and the heat release asymptotes to that of a nonpremixed flame ($\Phi = \infty$). For the richest stoichiometries ($\Phi \geq 4$), the premixed contribution is reduced to a "shoulder" on the left of the primary diffusion flame peak and a DF flame behavior dominates, with the flame positioned near the GSP. One can notice that the diffusion flame contribution is approximately always at the same position near the GSP. This is a consequence of maintaining constant the stoichiometric mixture fraction, Z_{st}.

The case $\Phi = 2.43$ shows a hybrid heat release with 67% of the total heat release generated by the premixed flame component and the remainder from the diffusion flame, confirming the hybrid nature of the flame. As shown in preliminary experiments, the flame exhibits a soot load that is compatible with diagnostic techniques. Therefore, this equivalence ratio is used in the experiments.

For such a flame we develop a complete database to understand the soot inception/growth process by quantifying soot optically and its gaseous precursors up to three-ring aromatics via gaseous sampling followed by chemical analysis to compare with chemistry models. Unlike the much richer flames that were explored recently in [16] in which the soot production was contributed mostly by the diffusion flame component, we will show that in the present case the premixed flame is the dominant contributor to soot and this PPF can be considered a perturbation of a purely premixed flame.

Table 1
Boundary conditions and flame parameters.

	Fuel Stream	Oxidizer Stream
C_2H_4	0.170	0.000
N_2	0.620	0.800
O_2	0.210	0.200
V_{avg}	26.3 cm/s	18.7 cm/s
V_{ax}	40.74 cm/s	26.17 cm/s
dV/dz	9.05 s^{-1}	46.66 s^{-1}
T	298 K	298 K
Z_{st}	$(1 + s\ Y_{rf}/Y_{OO})^{-1} = 0.40$	
a	$(V_{avg,f} + V_{avg,ox})/L = 45\ s^{-1}$	
Φ	2.43	
T_{max}	2230K	

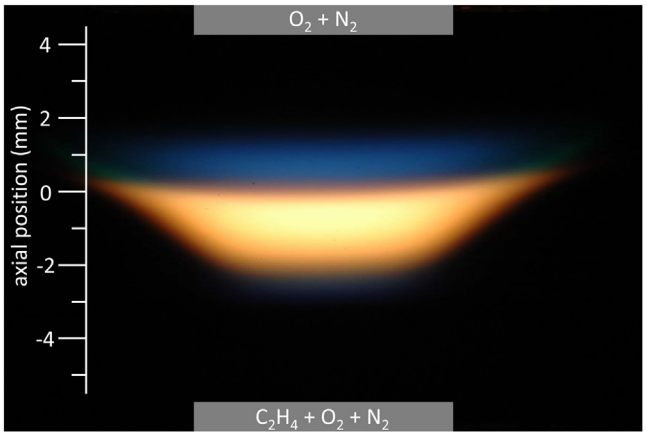

Fig. 2. Image of the PPF, with the burner nozzle exit indicated by the grey regions. The blue chemiluminescence of the PF is barely visible at the bottom unlike that of the DF that is at the top, with the soot layer sandwiched between the two.

2. Experimental and computational methods

Experiments are performed using a burner consisting of two opposed converging nozzles with 6.35 mm outlet diameter positioned $L = 10$ mm apart. Both nozzles are surrounded by conical enclosures conveying a nitrogen shroud flow to minimize external disturbances to the flame. Further details regarding the burner geometry are in [17]. Calibrated flows of ethylene/oxygen/nitrogen and oxygen/nitrogen are fed to the bottom and top nozzle, respectively, to stabilize a PPF at atmospheric pressure. The molar composition of the fuel and oxidizer streams are provided in Table 1. The mass average velocity of the two streams is 26.4 cm/s and 18.6 cm/s, to counteract the propagation of the PF component toward the fuel nozzle and position the entire PPF approximately centered between the two nozzles.

An image of the flame is shown in Fig. 2. A rich PF is stretch-stabilized with an opposite oxidizing stream, the residual fuel and combustion intermediates from the PF react with the counterflowing oxidizing stream to form a DF and produce ultimately a double flame structure. Soot is produced in the post flame of the PF and is eventually oxidized as it is convected toward the DF. Notice that even though the mixture fraction of the DF component, Z_{st}, is based on the mass fraction of the residual fuel, that is, unburnt C_2H_4, after complete conversion to CO_2 and H_2O from the PF component, we recognize that intermediate combustion products of the PF, such as CO and H_2, fuel the DF component [7,8], rather than the parent fuel. The DF is positioned near the GSP and slightly on the fuel side.

The selection of these flame conditions is based on several considerations:

(1) Ensuring that the equivalence ratio, Φ, fall in the range $2 < \Phi < 4$, which, in addition to being of relevance to compression-ignition engines [3,4], results in a hybrid flame in which both the premixed flame component and the diffusion flame component contribute to the heat release;
(2) Shifting the primary contribution to soot from the diffusion flame (see, [16]) to the premixed flame component of the PPF;
(3) Limiting the soot load and the maximum flame temperature to ensure compatibility with the diagnostic techniques; and
(4) Controlling the composition of the feed streams to position the diffusion flame component so that it oxidizes soot formed from the premixed flame component;

2.1. Experimental diagnostics

Key measurements include: temperature via a silica coated S-type thermocouple, gaseous sampling via a silica capillary probe, soot volume fraction and dispersion exponent via pyrometry, and soot particle size and number density by combing pyrometry measurements with light scattering measurements.

Thermocouple measurements are performed using a S-type thermocouple with a 125 μm diameter cylindrical bead. Experimental measurements are compared with the computed temperature profile by tracking optically the position of the peak chemiluminescence of the PF component relative to the thermocouple junction and overlapping it with the computed peak CH^* concentration. Standard corrections for radiative losses are applied on the basis of a convective-radiative energy balance. Thermocouple measurements are only performed outside of the soot forming region to compare the computed flame width and the experimentally measured one. The soot load of the flame, although moderate, is sufficiently high for particles to deposit quickly onto the junction which affect the thermocouples emissivity and diameter. Since these parameters are used to infer the temperature of the gas phase, the readings are unreliable in the soot forming region. The uncertainty in measured temperature is approximatley ±2%.

Gaseous sampling is performed using a silica capillary probe (OD/ID = 360 μm/180 μm) and GC/MS (Agilent 6890A/5973N) analysis to quantify H_2, O_2, N_2, CO, CO_2, and hydrocarbons up to three-ring PAH (166 amu). Details of the gaseous sampling are described exhaustively in [7,10,17] showing the capability to retain spatial resolution. Briefly, the probe is inserted radially into the flame and kept under vacuum to sample at several positions near the flame axis and the position of the probe tip relative to the PF chemiluminescent signal is monitored with a digital camera to overlap experimental data with the computed profiles. The sampling and storing system is kept at 423K to prevent condensation of heavy species. Gaseous calibration is performed with bottles (Scotty®) for species up to C4s, flow controllers for CH_4, C_2H_4, H_2, O_2, N_2, and electrosprayed liquid solutions of the compounds of interest that are completely vaporized in a stream of hot nitrogen. The cumulative error in measured concentrations is estimated at ±7.5% for light species (up to C2) and ±15% for the heavier ones by considering the uncertainties associated with calibration, sampling and analysis procedures.

Figure 3 shows the experimental layout for optical measurements. Soot volume fraction is measured via pyrometry using a Nikon D70 digital camera with a well characterized spectral response (400–700 nm) and a 210 mm focal length lens as described exhaustively in past work [18,19]. Data analysis is performed on an average of 20 images. An Abel transform deconvolves the line-of-sight images of each color channel (red, green, and blue) into two-dimensional fields and the ratio of any two Abel-transformed color channels is related to the intensity of radiation emitted through

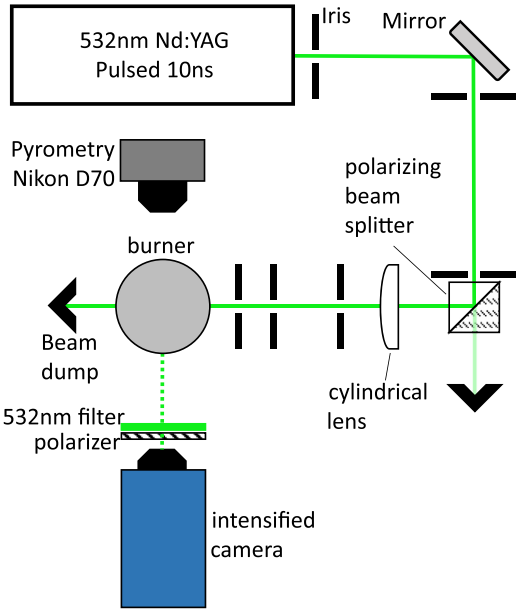

Fig. 3. Experimental layout for soot pyrometry and laser light scattering.

Planck's law

$$\frac{S_i}{S_j} = \frac{\int \eta_i(\lambda)\ \lambda^{-5+\alpha}\left[\exp\left(\frac{hc}{\lambda k_B T}\right)-1\right]^{-1} d\lambda}{\int \eta_j(\lambda)\ \lambda^{-5+\alpha}\left[\exp\left(\frac{hc}{\lambda k_B T}\right)-1\right]^{-1} d\lambda}. \quad (1)$$

The subscripts i and j refer to any of the three color channels. The overall optical efficiency is expressed with the wavelength dependent term $\eta(\lambda)$. The dispersion exponent, α, accounts for the soot emissivity which is assumed to follow a power-law dependence on wavelength, $\epsilon(\lambda) \sim \lambda^{-\alpha}$. Because of the large variability in the value of the dispersion exponent [18,20,21], Eq. (1) is used to evaluate the dispersion exponent, using the computed temperature profile that has been validated with thermocouple measurements.

The soot volume fraction is calculated using the following expression

$$f_v = -\frac{\lambda_e}{\tilde{K}_{ext} L_p}\ \ln\left\{1 - f_c(\lambda_e)\frac{\tau_c S_s}{\tau_s S_c} \times \exp\left[-\frac{hc}{k_B \lambda_e}\left(\frac{1}{T_c}-\frac{1}{T_s}\right)\right]\right\}, \quad (2)$$

where λ_e, L_p, τ, and $\tilde{K}_{ext}$ are the effective channel wavelength, pixel length, exposure time, and dimensionless extinction coefficient, respectively [22]. We assume $\tilde{K}_{ext} = 5.34 \pm 2.68$ which is estimated based on a range of reported values for the refractive index of soot [21]. The variability of the extinction coefficient with wavelength and soot maturity is lumped as general uncertainty. Subscripts 's' and 'c' refer to measurements on soot particles and light calibration source, respectively.

Planar light scattering measurements are performed with the (532 nm) second harmonic of a 10 ns pulsed Nd:YAG laser (New Wave Gemini PIV) as described in detail in [23]. Briefly, a cylindrical lens shapes the laser beam into a 7 mm by 0.8 mm sheet at the center of the burner with the laser fluence kept below 100 mJ/cm^2 to ensure that soot particles are not ablated by the high energy pulses. We repeated measurements in the 90-150 mJ/cm^2 range of laser fluency and verified that the measured particle sizes are independent of it (i.e., there are no errors from LII, PAH scattering, or soot particle vaporization), as documented in the SM. The lower limit of the laser fluence is chosen to resolve the Rayleigh scattering signal in the high temperature region. The scattered light is im-

aged onto an intensified camera (12-bit PCO DiCAM-Pro) through a polarizer and interference filter (532 nm ± 10 nm) positioned at a 90° scattering angle. Data analysis is performed on an average of 500 images captured in a 20 ns gating window centered around the triggering of the laser pulse. The gas-phase total light scattering coefficient of the investigated flames is calculated using the computed number concentration of H_2, H_2O, N_2, O_2, CH_4, CO, CO_2, C_2H_2, C_2H_4, C_2H_6, C_3H_8, C_3H_4, C_4H_6, and C_6H_6. All species accounted for in gas phase scattering, except for H_2O, are measured and quantified with the GC/MS. The temperature gradient in the soot forming zone of the investigated flame is relatively mild compared to typical counterflow flames and there is no evidence of beam steering.

Calibration gases (propane, ethylene, and nitrogen) are used to verify that the appropriate ratios of the scattering coefficient are obtained. The soot number concentration N_s is evaluated under the hypothesis of size monodispersity as

$$N_s = \frac{9\pi^2 F(m) f_v^2}{Q_{vv}^{soot} \lambda^4}, \quad (3)$$

where Q_{vv}^{soot} is the measured scattering coefficient attributed to soot, net of the Rayleigh scattering contribution from the gas phase, f_v is the measured soot volume fraction via pyrometry, and $F(m) = 0.69 \pm 0.13$ is the dimensionless refractive index function at the laser wavelength, $\lambda = 532$ nm, based on the relationship between F(m) and the dimensionless extinction coefficient, $\tilde{K}_{ext}$, at low laser fluence [24]. The soot particle diameter is assumed spherical and evaluated by $d = (6f_v/\pi N_s)^{1/3}$.

2.2. Flame modeling

One-dimension modeling of the flame is based on ANSYS CHEMKIN-Pro [14]. Multiple chemistry mechanisms are tested [25–27]. We account for multicomponent diffusion coefficients, thermal diffusion, and thermal radiation of CO, CO_2, H_2O, and CH_4 in the optically thin limit.

Previous work showed that it is essential to have correct boundary conditions to model properly both position and width of the flame [17]. To account for deviations from plug flow velocity boundary conditions, two-dimensional modeling is performed in ANSYS by modeling the flow within the converging nozzle burner and shroud housing, including reactions using a simple 5-step mechanism [7], mixture-averaged transport, and accounting for buoyancy. The computed axial velocity (V_{ax}) and velocity gradient (dV/dz) from the 2D simulations are provided in Table 1. Because we rely on simplified chemistry that was developed for DFs rather than PPFs, we model two-dimensionally a diffusion flame by replacing oxygen from the premixed stream with nitrogen and balancing the oxygen in the oxidizing stream to keep constant the stoichiometric mixture fraction. The rationale is that because the maximum flame temperature of the PPF is located at the DF, the thermal expansion of the PPF flame can be captured reasonably well by modeling a pure diffusion flame. The 2D simulation is not intended to replace the 1D simulation with detailed kinetics, but merely to improve the 1D simulation by accounting for deviations from plug flow boundary conditions [7,28].

3. Results and discussion

In Fig. 4 we compare thermocouple measurements with the computed temperature profile of three models: NBP from Narayanaswamy et al. [27], CRECK (C1-C16 HT+SOOT, Version 2003, March 2020) [25], and KAUST KM2 [26]. We register experimental and computational results by overlapping the chemiluminescent signal with the computed CH^* species profile of the premixed flame component [17]. The axial position is the same as the one sketched in Fig. 2: the premixed stream is on the left, the oxidizer stream on the right, with zero marking the position of the stagnation plane. The temperature profiles of all three models overlap in the DF region (z > 0 mm) and much of the soot forming/oxidizing zone (-3 mm < z < 0 mm), but there is some deviation near the PF with different predictions of the stretched laminar flame speed affecting the position of the premixed flame by less than 0.5 mm. There is no experimental data in the sooting region (-3 mm < z < -1 mm) because the intrusiveness of the thermocouple wire results in significant dragging of the premixed flame component and of soot deposition onto the thermocouple junction, affecting the measurements.

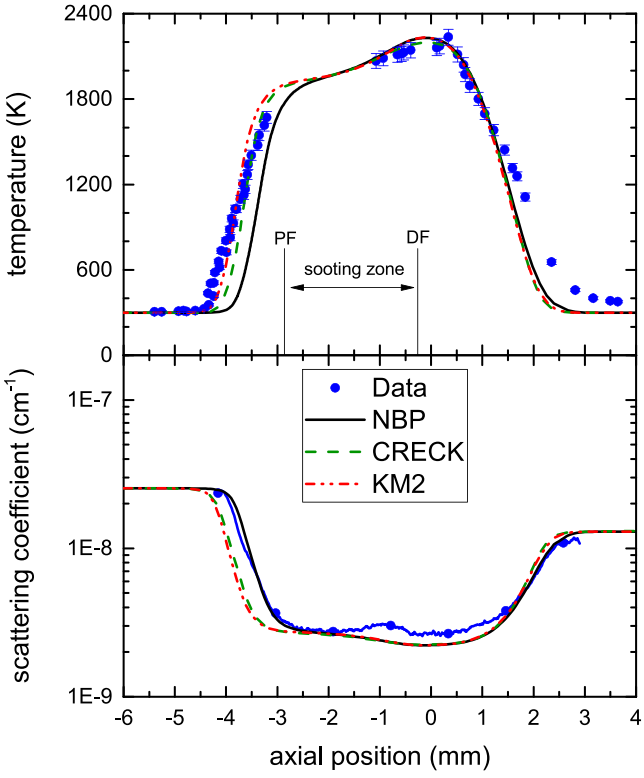

Fig. 4. Measured and computed profiles of temperature (top) and scattering coefficient (bottom). The PF and DF are labeled based on the computed local maximum CH^* mole fraction.

To complement the thermocouple measurements and rely on nonintrusive measurements, we also compare the measured Rayleigh scattering coefficient with the computed one. Thermocouple measurements may present a broader temperature profile [7,8], even in purely diffusion flames, which appears to be an issue in the oxidizer stream (z > 2 mm). Nonintrusive Rayleigh measurements, despite some uncertainties in molar composition, should provide an advantage to assess which model captures accurately the flame width. The NBP model [27], performs best with respect to the Rayleigh scattering measurements, whereas the thermocouple data validate the models ability to predict the peak flame temperature. There is some discrepancy between measured and computed scattering coefficient, because of the presence of soot as further discussed below. Benzene, the most abundant aromatic species, contributes less than 1% to the computed Rayleigh scattering signal of the gas phase. Because of the much lower concentration of larger aromatics, they would have an even smaller impact on the gas phase scattering despite having a larger (but unknown) cross section.

We show in Fig. 5 the measured and computed species profiles of the reactants, H_2, CO, CO_2, and C_2H_2 as further evidence that

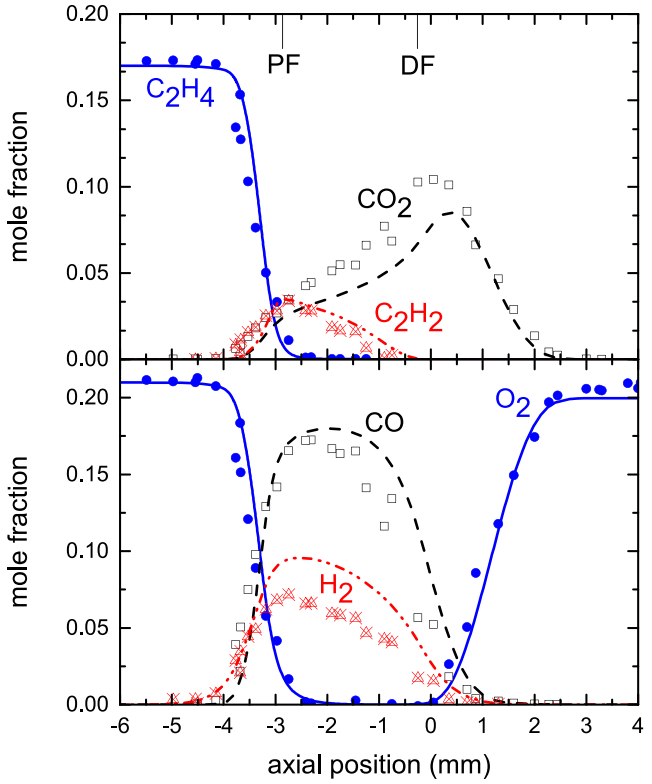

Fig. 5. Measured and computed profiles of C_2H_4, O_2, CO, CO_2, H_2, and C_2H_2.

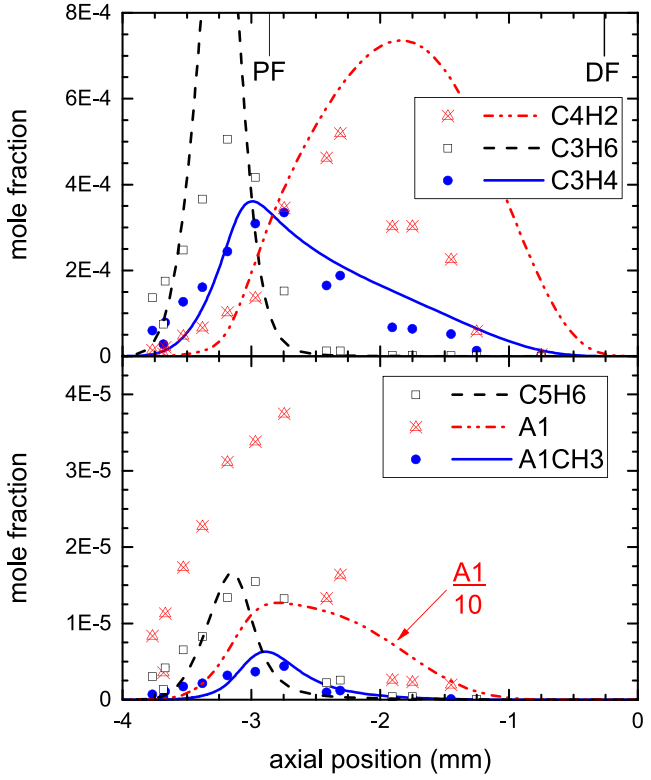

Fig. 6. Measured and computed profiles of some of the precursors to aromatic formation, benzene (A1), and toluene (A1CH3). Note that the computed A1 profile is divided by 10.

the overall flame width is well captured by the NBP mechanism when using the appropriate 2D velocity boundary conditions. We will be using only this mechanism [27] in the remaining discussion for clarity of presentation and compare different mechanisms in the supplemental material.

The gradients of the reactants (C_2H_4 and O_2) are well captured, even better than the thermocouple measurements in Fig. 4, attesting to the capability of sampling to retain good spatial resolution. C_2H_4 is consumed in the PF component, with CO and H_2 feeding the DF component as observed in past studies on PPFs [7,8,10]. H_2 is overpredicted by the model, similar to the case of premixed flames [18,29], which may be due to an overly pronounced role of H-abstraction reactions. Nevertheless, the model captures qualitatively the decrease in H_2 approaching the DF component. Acetylene, a key component in the growth of PAHs and soot, is primarily formed in the post flame region of the PF and gradually consumed in the soot forming region and is also well captured by the model.

Critical intermediate species to aromatic formation are shown in Fig. 6. Propylene (C_3H_6) is produced primarily from the PF and quickly consumed. C_3H_4, lumping propyne and allene as key isomers in the formation of propargyl radical (C_3H_3), survives in appreciable amount in the post flame region, while diacetylene (C_4H_2) is produced further downstream of the PF. Benzene (A1) is primarily formed via propargyl radical recombination and is measured to be in comparable concentration as C_3H_4, but is overpredicted by the model by a factor of 3. Our GC/MS is limited to quantifying stable species, but in view of the agreement of C_3H_4 and C_5H_6, the stable intermediates to propargyl radical formation, the overly pronounced role of H-abstraction and subsequent overprediction of H_2 in Fig. 5 may explain the overprediction of benzene. Toluene (A1CH3), on the other hand, is measured to be approximately one order of magnitude lower in concentration than benzene and is well captured by the model.

Methylated aromatic species and PAHs are shown in Fig. 7. Most of the methylated aromatic species are formed near the PF and are quickly depleted, which is well predicted by the model. Naphthalene is measured to be approximately two orders of magnitude lower in concentration as compared to benzene, but is overpredicted by approximately one order of magnitude. Methylnaphthalene is one order of magnitude lower than naphthalene and is well captured, following a similar trend as benzene and toluene in Fig. 6. All aromatic species peak just downstream of the PF component (at approximately $z = -3$ mm) and are consumed approaching the DF component. Excluding benzene and naphthalene, which are arguably among the most critical species to predict soot formation, the model performs well at predicting the experimental data.

The concentration of aromatic species in the post flame region of a premixed flame have been measured to reach a steady state [18,30]: the formation rate is approximately balanced with the destruction rate so that the species molar fraction plateau. In the current PPF, there is a significant source of OH radicals from the DF component as shown in Fig. 7, which implies that the DF introduces an oxidizing environment downstream of the PF. This flame structure is distinctly different from that of PPFs with much richer equivalence ratios and low mixture fractions [7,9,10]. In the latter case, PPFs are perturbations of a diffusion flame and exhibit a 'merged' flame in contrast with the present distinct double flame structure [8]. In the 'merged' flame, partial premixing tends to increase the temperature of the soot forming zone and boost soot production from the DF at constant Z_{st} [7,9]. At sufficiently low equivalence ratios (e.g., $\Phi \leq 5$), the PF component is distinct and soot is formed on both sides of the stagnation plane [7,16]. Here, we observe that at an equivalence ratio relevant to CI-engines [3,4] ($\Phi < 4$) the PPFs appears to be a perturbation of PF, suggesting that there is a critical Φ determining whether the PF or the DF is the dominant flame component in these double flame structures.

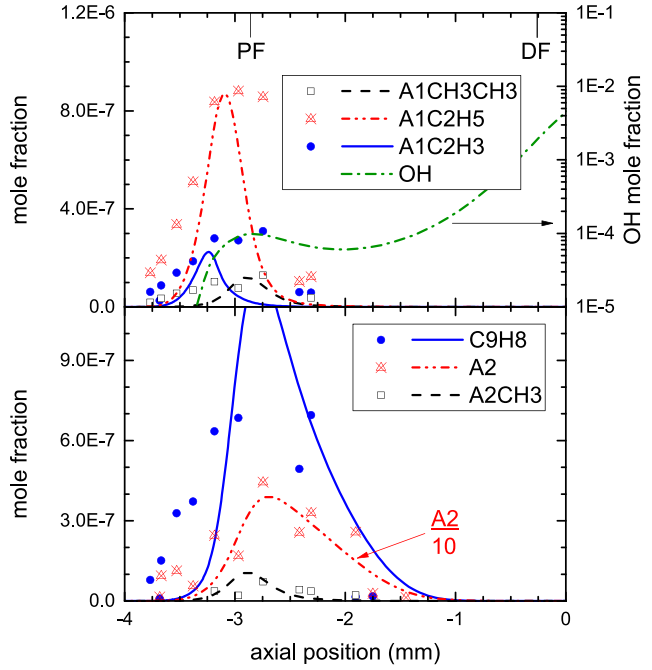

Fig. 7. Measured and computed profiles of some aromatic species: Xylene (A1CH3CH3), ethylbenzene (A1C2H5), styrene (A1C2H3), indene (C9H8), naphthalene (A2), and methylnaphthalene (A2CH3). Note that the computed A2 profile is divided by 10.

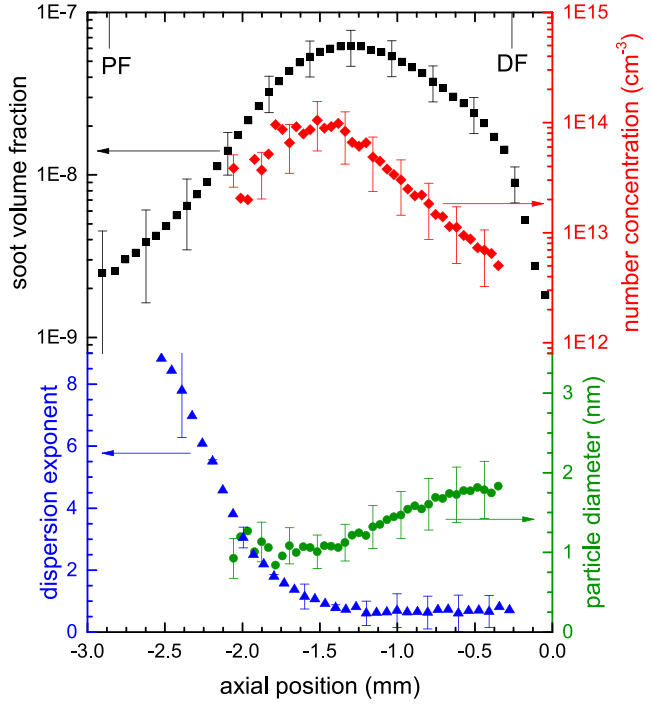

Fig. 8. Measured soot volume fraction, dispersion exponent, number concentration, and particle size.

We complement the quantification of gaseous soot precursors with soot measurements in Fig. 8. Soot nucleates near the PF component (z = -3 mm) at a computed flame temperature of approximately $T = 1700$ K and with large values of the dispersion exponent. The volume fraction increases by nearly two orders of magnitude, as the dispersion exponent monotonically decreases until it reaches a plateau near $\alpha = 0.7$, similar to the behavior at atmospheric pressure [20] and in low-pressure burner-stabilized premixed flames [31]. However, it is worth emphasizing the difference in temperature-time history compared to typical burner-stabilized premixed flames: while soot nucleates at nearly the same temperature ($T = 1700$ K), the temperature monotonically increases in this PPF (from PF to DF, left to right in Fig. 8) as particle residence time increases, unlike burner-stabilized premixed flames whose temperature gradually decreases because of heat loss. Nevertheless, the observed trends in soot nucleation and particle growth further corroborates the notion that this PPF has a more distinct premixed flame character compared to PPFs at higher equivalence ratios [16].

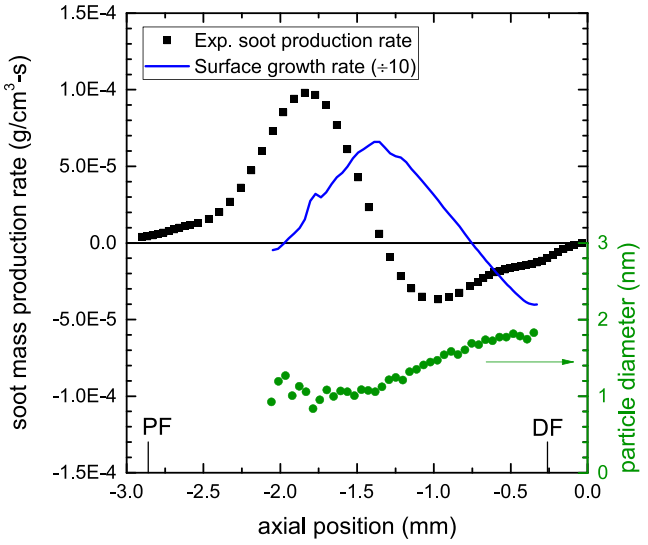

Fig. 9. Experimentally measured soot production rate, surface growth rate, and measured particle diameter.

Approximately half way between the PF and the DF (z = -1.5 mm) the soot volume fraction begins to decrease as it is oxidized by the DF component, with the dispersion exponent remaining unaffected. Rayleigh scattering by soot is first detected at approximately z = -2 mm, with nascent particles being undetected for -3 mm < z < -2 mm. The number concentration profile qualitatively resembles that of the volume fraction – there is an initial increase in number concentration as particles are nucleated, followed by a decrease at z = -1.5 mm as particles coagulate and/or experience oxidation approaching the DF component. The particle size increases with increasing residence time but remains small at a few nanometers, suggesting that the assumption of monodisperse size distribution remains valid.

The soot mass balance equation considering both thermophoretic and Brownian effects is

$$\dot{\omega}_s = \frac{d}{dz}(\rho Y_s(V_{ax} + V_{th} + V_P)) + \rho Y_s \frac{dV_r}{dr}. \quad (4)$$

In Eq. (4), ρ and dV_r/dr are the gas density and radial gradient of the radial velocity computed with the 1-D model, Y_s is the mass fraction of soot as $Y_s = \rho_s f_v/\rho$ using an assumed soot density $\rho_s = 1.5$ g/cm^3 and the measured soot volume fraction. The Brownian velocity is estimated by $V_P = -D_P \cdot d\ln(Y_s)/dz$. The value of the Brownian diffusivity is calculated as a function of the measured particle diameter d [23].

Profiles of the soot production rate, computed net surface growth (including oxidation) rate and particle diameter are shown in Fig. 9. Surface growth is modeled by acetylene addition [32], by assuming a steric factor (i.e., the probability of successful chemisorption) of 0.7. Oxidation by OH is assumed to have a collision frequency of 0.13 [33], whereas oxidation by O_2 is based on an empirically derived expression [34]. Soot is formed in the post flame region of the PF component, with the production rate

increasing as the temperature increases. As the particle residence time increases and particles approach the DF component, the soot production rate drops and becomes negative.

In previous investigations [16], oxidation of PPFs was primarily by O_2. Surface growth dominates over the oxidation rate close to the PF with the oxidation by O_2 dominating at $z < -1.5$ mm. On the other hand, oxidation by OH dominates at $z > -1.5$ mm, where the mass production is negative. Therefore, predicting accurately the soot growth and oxidation in PPFs requires accurate modeling of both O_2 and OH. Data comparing the individual oxidation rates are provided in the supplemental material. We note that perhaps because of diagnostic limitations, we measure a monotonic increase in particle size, where one would expect a decrease as oxidation takes over. The measured increase is consistent with the computed surface growth rates with a net positive growth rate throughout most of the soot forming region in spite of the calculated decrease is mass production rate at $z > -1.3$ mm. We did not consider the uncertainty in the assumed steric factor or collision frequency, which may influence where OH oxidation begins to dominate over C_2H_2 growth. The integration of Eq. (4) in (particle residence) time along the traverse direction, where the residence time is the integral of the inverse sum of axial, thermophoretic and Brownian velocities, yields approximately zero, which confirms that all of the soot that is produced by the PF component is oxidized by the DF with hardly any soot being convected away radially at the stagnation plane.

4. Conclusions

Detailed measurements in a partially premixed atmospheric pressure counterflow diffusion flame of ethylene are reported. The flame investigated has an equivalence ratio $\Phi = 2.43$ with flame conditions precisely controlled to allow for the quantification of both chemical species and soot. Principal conclusions follow.

- The relatively low equivalence ratio of the PPF led to distinct PF and DF components. The high Z_{st} positioned the diffusion flame on the fuel side of the stagnation plane to produce a soot oxidizing environment and mimic the flame environment observed in CI-engines.
- Unlike previous studies on PPFs at $\Phi \geq 5$ which were considered to be perturbation of a pure diffusion flame, the lower Φ and higher Z_{st} of the investigated flame makes the premixed flame the dominant contributor to soot. Thus, this PPF can be considered as a perturbation of a purely premixed flame.
- Soot precursors are primarily formed in the post flame region of the premixed flame, with their peak mole fraction positioned close to the premixed flame, and decrease in mole fraction approaching the diffusion flame. With the exception of two critical species, benzene and naphthalene, the NBP model performs well at predicting the experimental data.
- Soot nucleates near the PF with large values of the dispersion exponent. With increasing residence time, particles are convected toward the diffusion flame while the dispersion exponent decreases until it reaches a plateau of $\alpha = 0.7$ and the volume fraction first increases and then decreases, as it is consumed by oxidation. Particle size is measured to increase continuously, but remains within a few nanometers throughout the soot forming region.
- Soot production rate is evaluated from the measured volume fraction and confirms that soot production is dominated by the premixed flame and that soot is oxidized at the diffusion flame. Virtually all soot is consumed by oxidation via OH at the diffusion flame with no soot being convected away radially at the stagnation plane.

Declaration of Competing Interest

The authors declare that they have no known competing financial interests or personal relationships that could have appeared to influence the work reported in this paper.

Acknowledgments

The authors acknowledge the support of the National Science Foundation (CBET-1853150). Authors declare no competing interests.

Supplementary materials

Supplementary material associated with this article can be found, in the online version, at doi:10.1016/j.combustflame.2022.112429.

References

[1] Y. Wang, S.H. Chung, Soot formation in laminar counterflow flames, Prog. Energy Combust. Sci. 74 (2019) 152–238.
[2] H. Wang, Formation of nascent soot and other condensed-phase materials in flames, Proc. Combust. Inst. 33 (2011) 41–67.
[3] J.E. Dec, A conceptual model of DI diesel combustion based on laser-sheet imaging, SAE Tech. Pap. 970873 (1997).
[4] J.E. Dec, Advanced compression-ignition engines—understanding the in-cylinder processes, Proc. Combust. Inst. 32 (2009) 2727–2742.
[5] N. Peters, Turbulent Combustion, IOP Publishing, 2001.
[6] A.R. Masri, Partial premixing and stratification in turbulent flames, Proc. Combust. Inst. 35 (2015) 1115–1136.
[7] F. Carbone, F. Cattaneo, A. Gomez, Structure of incipiently sooting partially premixed ethylene counterflow flames, Combust. Flame 162 (2015) 4138–4148.
[8] P. Berta, S.K. Aggarwal, I.K. Puri, An experimental and numerical investigation of n-heptane/air counterflow partially premixed flames and emission of NOx and PAH species, Combust. Flame 145 (2006) 740–764.
[9] L. Xu, F. Yan, M. Zhou, Y. Wang, An experimental and modeling study on sooting characteristics of laminar counterflow diffusion flames with partial premixing, Energy 218 (2021) 119479.
[10] F. Carbone, K. Gleason, A. Gomez, Pressure effects on incipiently sooting partially premixed counterflow flames of ethylene, Proc. Combust. Inst. 36 (2017) 1395–1402.
[11] H.P. Mungekar, A. Atreya, Effect of partial premixing on the sooting structure of methane flames, Combust. Flame 144 (2006) 336–348.
[12] H.P. Mungekar, A. Atreya, Flame radiation and soot emission from partially premixed methane counterflow flames, J. Heat Transf. 128 (2006) 361.
[13] J.Y. Hwang, S.H. Chung, Growth of soot particles in counterflow diffusion flames of ethylene, Combust. Flame 125 (2001) 752–762.
[14] A.N.S.Y.S. CHEMKIN-Pro Release 2019 R2, 2022.
[15] H. Wang, X. You, A. V. Joshi, S.G. Davis, A. Laskin, F.N. Egolfopoulos, C.K. Law, USC Mech version II. High-temperature combustion reaction model of H2/CO/C1-C4 Compounds, http://ignis.usc.edu/USC_Mech_II.htm (2007).
[16] K. Gleason, F. Carbone, A. Gomez, Effect of equivalence ratio and temperature on soot formation in partially premixed counterflow flames, Combust. Flame 242 (2022) 112088.
[17] L. Figura, F. Carbone, A. Gomez, Challenges and artifacts of probing high–pressure counterflow laminar diffusion flames, Proc. Combust. Inst. 35 (2015) 1871–1878.
[18] F. Carbone, K. Gleason, A. Gomez, Probing gas-to-particle transition in a moderately sooting atmospheric pressure ethylene/air laminar premixed flame. Part I: gas phase and soot ensemble characterization, Combust. Flame 181 (2017) 315–328.
[19] K. Gleason, F. Carbone, A. Gomez, Pressure and temperature dependence of soot in highly controlled counterflow ethylene diffusion flames, Proc. Combust. Inst. 37 (2019) 2057–2064.
[20] J. Simonsson, N.E. Olofsson, S. Török, P.E. Bengtsson, H. Bladh, Wavelength dependence of extinction in sooting flat premixed flames in the visible and near-infrared regimes, Appl. Phys. B Lasers Opt. 119 (2015) 657–667.
[21] K. Gleason, F. Carbone, A. Gomez, Effect of temperature on soot inception in highly controlled counterflow ethylene diffusion flames, Combust. Flame 192 (2018) 283–294.
[22] F. Cignoli, S. De Iuliis, V. Manta, G. Zizak, Two-dimensional two-wavelength emission technique for soot diagnostics, Appl. Opt. 40 (2001) 5370–5378.
[23] K. Gleason, F. Carbone, A. Gomez, PAHs controlling soot nucleation in 0.101—0.811MPa ethylene counterflow diffusion flames, Combust. Flame 227 (2021) 384–395.
[24] H.A. Michelsen, P.E. Schrader, F. Goulay, Wavelength and temperature dependences of the absorption and scattering cross sections of soot, Carbon 48 (2010) 2175–2191.

[25] CRECK C1-C16 high temperature (HT+SOOT) mechanism: http://creckmodeling.chem.polimi.it/menu-kinetics/menu-kinetics-detailedmechanisms/107-category-kinetic-mechanisms/402-mechanisms-1911-tot-ht.
[26] Y. Wang, A. Raj, S.H. Chung, A PAH growth mechanism and synergistic effect on PAH formation in counterflow diffusion flames, Combust. Flame 160 (2013) 1667–1676.
[27] K. Narayanaswamy, G. Blanquart, H. Pitsch, A consistent chemical mechanism for oxidation of substituted aromatic species, Combust. Flame 157 (2010) 1879–1898.
[28] P. Jiang, M. Zhou, D. Wen, Y. Wang, An experimental multiparameter investigation on the thermochemical structures of benchmark ethylene and propane counterflow diffusion flames and implications to their numerical modeling, Combust. Flame 234 (2021) 111622.
[29] W. Pejpichestakul, A. Cuoci, A. Frassoldati, M. Pelucchi, A. Parente, T. Faravelli, Buoyancy effect in sooting laminar premixed ethylene flame, Combust. Flame 205 (2019) 135–146.
[30] M.J. Castaldi, N.M. Marinov, C.F. Melius, J. Huang, S.M. Senkan, W.J. Pitz, C.K. Westbrook, Experimental and modeling investigation of aromatic and polycyclic aromatic hydrocarbon formation in a premixed ethylene flame, Proc. Combust. Inst. 26 (1996) 693–702.
[31] G. Cléon, T. Amodeo, A. Faccinetto, P. Desgroux, Laser induced incandescence determination of the ratio of the soot absorption functions at 532 nm and 1064 nm in the nucleation zone of a low pressure premixed sooting flame, Appl. Phys. B Lasers Opt. 104 (2011) 297–305.
[32] M. Frenklach, H. Wang, Detailed modeling of soot particle nucleation and growth, Proc. Combust. Inst. 23 (1991) 1559–1566.
[33] K.G. Neoh, J.B. Howard, A.F. Sarofim, D.C. Siegla, Soot oxidation in flames, Particulate Carbon: Formation During Combustion (Ed.), Springer, 1981, pp. 261–282.
[34] J. Nagle, R.F. Strickland-Constable, Oxidation of carbon between 1000-2000C, Proc. Fifth Carbon Conf. 1 (1962) 154–165, doi:10.1016/B978-0-08-009707-7.50026-1.